Engineering Colloidal Lithography and Nanoskiving to Fabricate Rows of Opposing Crescent Nanogaps

Gu, Panpan; Zhang, Wei; Zhao, Zhiyuan; Ai, Bin; Zheng, Tianxing; Chiechi, Ryan C.; Li, Chunguang; Shi, Zhan; Zhang, Gang

IMPORTANT NOTE: You are advised to consult the publisher's version (publisher's PDF) if you wish to cite from it. Please check the document version below.

Link to publication in University of Groningen/UMCG research database

Check for updates

Engineering Colloidal Lithography and Nanoskiving to Fabricate Rows of Opposing Crescent Nanogaps

Panpan Gu, Wei Zhang, Zhiyuan Zhao, Bin Ai, Tianxing Zheng, Ryan C. Chiechi, Chunguang Li, Zhan Shi, and Gang Zhang*

A scalable fabrication route combining colloidal lithography and nanoskiving is reported for generating free-standing asymmetric metal nanostructures of crescent-shaped gold nanowires and rows of opposing crescents with and without nanogaps. Strong localized surface plasmon resonances and propagating surface plasmon polaritons are excited at the sharp tips of the crescent and in the sub-10 nm nanogaps. High-order resonance modes are excited due to the coupling between the resonances in the tips and gaps. The Raman signals are greatly enhanced due to the strong electric fields. In addition, the optical responses and electric field distributions can be controlled by the polarization of the incident light. The strong electric field enhancement coupled with facile, scalable fabrication make crescent-shaped nanostructures promising in nonlinear optics, optical trapping, and surface-enhanced spectroscopy.

Dr. P. Gu, W. Zhang, T. Zheng, Prof. G. Zhang
State Key Lab of Supramolecular Structure and Materials
College of Chemistry
Jilin University
Changchun 130012, P.R. China
E-mail: gang@jlu.edu.cn
Dr. P. Gu
Present address: College of Chemical Engineering and Machinery
Eastern Liaoning University
Dandong 118003, P. R. China
Dr. Z. Zhao
Institute of New Energy on Chemical Storage and Power Sources
College of Applied Chemistry and Environmental Engineering
Yancheng Teachers University
Yancheng 224002, P. R. China
Dr. B. Ai
School of Microelectronics and Communication Engineering
Chongqing Key Laboratory of Bio-perception and Intelligent
Information Processing
Chongqing University
Chongqing 400044, P. R. China
Prof. R. C. Chiechi
Stratingh Institute for Chemistry, and Zernike
Institute for Advanced Materials
University of Groningen
Nijenborgh 4, Groningen, AG 9747, The Netherlands
Dr. C. Li, Prof. Z. Shi
State Key Laboratory of Inorganic Synthesis and Preparative Chemistry
College of Chemistry
Jilin University
Changchun 130012, P. R. China

The ORCID identification number(s) for the author(s) of this article can be found under https://doi.org/10.1002/adom.202000006.

1. Introduction

Plasmonic nanostructures have attracted considerable attention due to their ability to manipulate light and their potential for widespread applications, such as surface enhanced spectroscopies,[1–6] biosensors,[7–9] and nonlinear optics.[10–12] A currently fast developing area in plasmonics is metal nanoparticles. They have great applications in sensing,[13] imaging,[14] catalysis,[14–17] biomedicine,[18,19] etc. In particular, asymmetric nanoparticles have unique optical properties, which are different from their normal symmetrical nanostructures.[20–22] Plasmonic nanocrescents, a representative asymmetric nanostructure, have been deeply studied and shown a series of meaningful optical properties. For example, the dark-mode plasmon resonances on crescent-shaped nanostructures show interesting applications in engineering metamaterials,[23] surface enhanced spectroscopy,[3,24–26] improving the refractive index sensitivity of sensors,[21,27] and optical trapping.[28,29] Also the multipolar Fano resonance in the symmetry breaking nanocrescent is important for nonlinear optics.[20,22] In view of its remarkable advantages and wide application prospects, many efforts have been made to produce various plasmonic nanocrescents.[3,26,30–32] Shumaker–Parry's research group reported that the gold crescent-shaped nanoantennas exhibited localized surface plasmon resonances (LSPRs) in infrared and also the LSPRs are sensitive to the structural parameters and the local dielectric environment.[33] Maximilian Kreiter et al. prepared opposing nanocrescent dimers with strong electric field enhancements at the nanogap between the opposing crescent tips (OCTs).[31]

Typically, plasmonic nanocrescents are fabricated by serial top-down methods, such as electron beam lithography (EBL).[21,34] Although this approach can produce high precision and controllable nanocrescents, it generally suffers from high cost and low throughput, which hinders their applications. In addition, it is difficult to use EBL to produce structures with nanoscale sharp tips. For industrial scale production, a number of crescent-shaped nanostructures have been prepared via colloidal lithography (CL),[26,30,35] nanoimprint lithography (NIL),[36,37] and nanotransfer printing.[38] CL uses monolayers of non-close packed nanospheres as mask to determine the diameter of crescent. The metal deposition

ADVANCED
SCIENCE NEWS
www.advancedsciencenews.com

ADVANCED
OPTICAL
MATERIALS
www.advopticalmat.de

angle is varied to control the distance of the tips (opening) in crescents and its symmetry. However, the deposition incident angle and azimuth angle must be precisely controlled.[31,39] In the nanotransfer printing method, nanocrescent structures are fabricated by transfer printing with oblique shadow metal deposited polydimethylsiloxane (PDMS) stamps. Their sizes are adjusted by controlling the printing pressure.[38] The crescent-shaped nanostructures can also be fabricated by deflected capillary force lithography (dCFL).[40] The nanocrescents are formed by the deflection of PDMS pillars under shear force. However, it is difficult to fabricate crescent-shaped nanostructures with sub-10 nm nanogaps or crescent dimers with opposing tips using those nanofabrication techniques; and these structures are expected to have stronger electric field enhancements due to the integrated hot spots of tips and gaps.

Herein, we combined colloidal lithography and nanoskiving (CL-nanoskiving)[41–43] to develop a novel low-cost method for preparing different types of crescent-shaped plasmonic nanostructures. In contrast to the previous periodic crescent nanogap arrays,[44] our crescent nanostructures were fabricated based on close-packed nanospheres and vertical physical sectioning. Gold crescent nanowires (CNWs) with sub-10 nm sharp tips are designed, fabricated, and characterized. Not only LSPRs, but also propagating surface plasmon polaritons (SPPs) are excited in the CNWs. The coupling of the two plasmonic modes further enhances the electric fields. In addition, crescent nanogaps (CNGs) are fabricated by multiple deposition techniques. The sub-10 nm nanogaps in CNGs can squeeze and confine light, leading to extreme electric field enhancement. Notably, the opposing crescent nanowires (OCNWs) and opposing crescent nanogaps (OCNGs), which are hard to obtain by conventional fabrication techniques, can be easily fabricated by a simple opposite deposition procedure. These nanostructures possess denser hot spots, leading to stronger electric fields and higher Raman signals.

2. Results and discussion

2.1. Fabrication of CNWs and CNGs

The proposed CL-nanoskiving technique consists of four main steps: i) self-assembly of monolayer colloidal crystals, ii) vertical deposition of metals, iii) embed in epoxy, and iv) section by an ultra-microtome. As illustrated in **Figure 1**, at first, 3 nm chromium film was vertically deposited on silicon substrate to increase the adhesion between gold and silicon substrate. Then close-packed monolayer colloidal crystals were assembled on the substrate surface by interface method (Figure 1a) to form the template.[45–47] The gold was deposited on the as-prepared substrate by a vertically thermal evaporator (Figure 1b) and the epoxy was cured onto the substrate to peel off the gold-coated nanosphere arrays, leaving behind metal nanotriangle arrays on the substrate (Figure 1c). Then the gold-coated nanosphere arrays were embedded in more epoxy to form blocks (Figure 1d). After that, the samples were sliced into ultrathin sections by an ultra-microtome, in which the diamond knife was parallel to the crystal lattice direction (Figure 1e). The slab was transferred onto a gold film (Figure 1f). The CNWs were obtained after removing epoxy and nanospheres by reactive ion etching (RIE) (Figure 1g). Note that, it will cause constructive interference between the incident and reflected light by introducing the gold reflective mirror, then leading to significant electric field enhancement. On the contrary, if the crescent nanostructures were directly in contact with the bulk silicon substrate, it will cause a broad spreading of the local electric field, the final electric field will be weakened to a large extent.[48,49] **Figure 2**a,b show scanning electron microscopy (SEM) images of a typical CNWs with the period (P) of 700 nm and the average thickness (T) of about 110 nm. From the zoomed-in image (Figure 2b), the integrity of the CNWs can be clearly seen. Each typical region of the CNWs has sharp tips with the tip curvature radius of ≈10 nm, as shown in Figure 2b. Noted that the blocks containing the gold-coated nanosphere
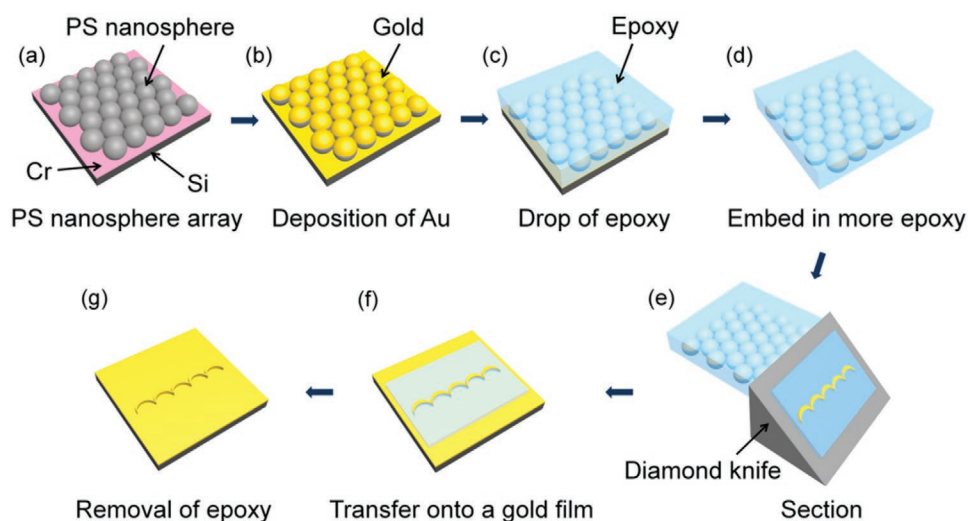
Figure 1. Schematic illustration of the process used to fabricate the CNWs. a) Close-packed colloidal crystals are assembled onto the silicon wafer with a thin chromium layer. b) Vertical deposition of gold film on substrate. c) The epoxy is dropped onto the substrate. d) Embedding the sample in more epoxy. e) Vertical section by ultra-microtome. f) Transfer of one section onto a gold film. g) Removing of the epoxy and nanospheres by RIE.
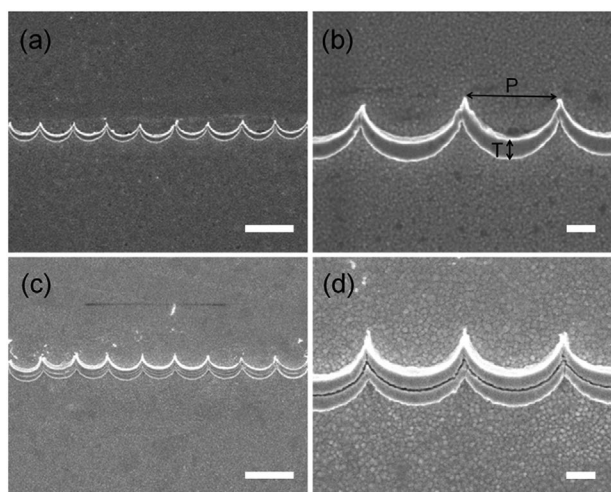
Figure 2. a) Typical SEM image of CNWs with $P = 700$ nm and $T = 110$ nm. b) Zoomed-in SEM image of (a). c) SEM image of CNGs. d) Zoomed-in SEM image of (c). The scale bars: 1 µm in (a), (c), and 200 nm in (b), (d).

arrays were sectioned continuously, this would lead to CNWs with different size. Herein, the largest CNWs obtained by sectioning through the diameter were studied. Though the CNWs with fixed dimensions are fabricated here, the inner diameter (P) and thickness (T) of the CNWs can be controlled by the size of the nanosphere template and the deposition thickness of the gold film, respectively. The structures of the CNWs retain its original shape in the process of transferring them onto a substrate for imaging and removing the sacrificial nanosphere template.[43,44] The large area SEM image of CNWs is shown in Figure S1a, Supporting Information, it demonstrates the long axis nanostructures can be obtained via the combination of colloidal lithography and nanoskiving technique.

Nanogaps between two noble metal nanostructures can "squeeze" light, leading to extreme confinement of electro–magnetic energy, which can significantly enhance the surface enhanced Raman scattering (SERS) of detection molecules adsorbed in the nanogaps.[50,51] Benefiting from the advantages of the conventional thin film deposition technology, we have successfully fabricated CNGs, which are comprising two parallel crescent-shaped nanowires with a spacing of sub-10 nm. The fabrication process is successively depositing gold (110 nm)/aluminum (4 nm)/gold (110 nm) sandwich films on the close-packed colloidal monolayer in the deposition step (Figure 1b) and then perpendicularly section the sample by ultra-microtome. After the removal of the sacrificial aluminum layer, epoxy, and nanospheres, CNGs with sub-10 nm nanogaps are fabricated. The gap-width can be adjusted by the thickness of aluminum. In addition, silica, grapheme,

and aluminum trioxide can also be used as the sacrificial layers. The SEM images in Figure 2c,d show that the uniform CNGs with sub-10 nm nanogaps have been successfully fabricated in a long range (more large area CNGs in Figure S1b, Supporting Information).

2.2. Fabrication of OCNWs and OCNGs

The structure morphology of the crescent nanowires have a great influence on their optical properties, because the plasmon resonance is sensitive to small changes in the geometry of the crescents.[52] To obtain crescent nanostructures with strong optical properties, the OCNWs were fabricated by re-depositing metals on the opposite side of the colloidal crystals film, and then slicing. **Figure 3** outlines the fabrication process of the OCNWs nanostructures. Briefly, after a Cr adhesion layer was deposited on the silicon substrate, close-packed colloidal crystals were then assembled on the as-prepared substrate surface by interface method (Figure 3a). A gold film with a thickness of 110 nm was deposited on the colloidal crystals (Figure 3b). After the gold-coated nanosphere arrays were peeled off with scotch tape (Figure 3c), another gold film was deposited on the opposite side of the gold-coated nanosphere arrays (Figure 3d). Then the epoxy was dropped onto the substrate to peel off the two opposite side gold-coated nanosphere arrays (Figure 3e). The two opposite side gold-coated nanosphere arrays were embedded in more epoxy (Figure 3f). The samples were sliced
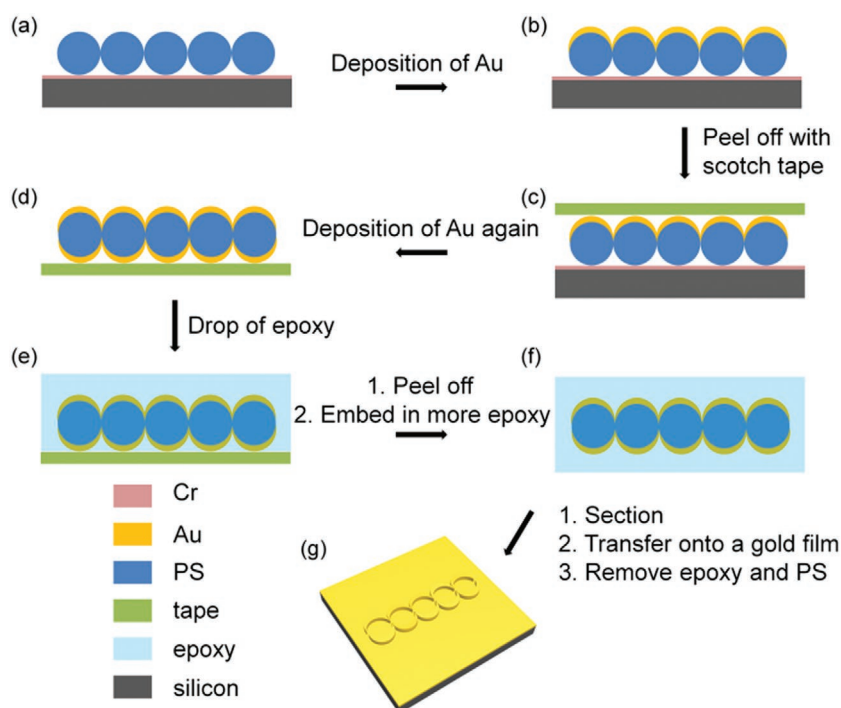
Figure 3. Outline of the process to fabricate the OCNWs. a) Close-packed colloidal crystals are assembled onto the silicon wafer with a thin chromium layer. b) Then gold film is deposited vertically on the substrate.c) The gold-deposited nanosphere arrays are peeled off with scotch tape. d) Another gold film is deposited onto the opposite side of the gold-coated nanosphere arrays. e) The epoxy is dropped onto the substrate to peel off the two opposite side gold-deposited nanosphere arrays. f) Embedding the sample in more epoxy. g) Removal of epoxy and nanospheres by RIE.

2000006 (3 of 8)
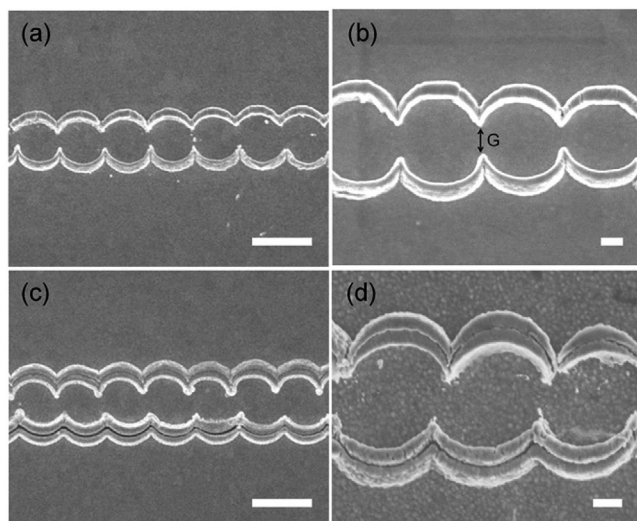
Figure 4. Typical SEM images of a) OCNWs in a large range and b) the magnified SEM image. c) SEM image of the OCNGs. d) Enlarged SEM image of (c). The scale bars: 1 μm in (a), (c) and 200 nm in (b), (d).

into ultrathin sections by an ultramicrotome, which were then transferred onto a gold film. The OCNWs were formed after removal of epoxy and nanospheres by RIE (Figure 3g).

Figure 4a shows that the OCNWs are fabricated uniformly in a large range. Figure 4b provides a highly magnified SEM image of the OCNWs, which presents clear crescent shapes with sharp tips, and proves that the crescent nanowires are continuous and have no defects in a large range(more large area OCNWs in Figure S1c, Supporting Information). The gap (G) between the opposing tips is 180 nm (Figure 4b), thus coupling effects between the two OCNWs are expected. Moreover, a smaller gap-width could be obtained by an additional slight RIE to decrease the contact area between the PS nanospheres (Figure S2, Supporting Information). From the previous discussion, we know that the crescent nanogaps can squeeze and focus light through the gaps and sharp tips. The coupling between the nanogaps and tips leads to extreme electric field enhancement in the tipped-nanogaps, resulting in potential applications in, for example, surface-enhanced spectroscopy.[43] Here, we fabricated a crescent nanogaps dimer consisting of two crescent nanogaps with opposing tip, termed as OCNGs.

The fabrication process is to successively deposit gold (110 nm)/ aluminum (4 nm)/gold (110 nm) sandwich films on the close-packed colloidal monolayer in the deposition step (Figure 3b,d). Figure 4c,d show that the OCNGs have been successfully fabricated. It demonstrates that the OCNGs with opposing tips and sub-10 nm gaps are uniform in a long range (more large area OCNGs in Figure S1d, Supporting Information).

2.3. Optical Performance of Crescent-shaped Nanostructures

The prepared crescent-shaped nanostructures in this paper are unique in electric field distributions compared with other similar crescent nanostructures because they have periodic crescent tips along the nanowires, which allows effective electric field enhancement caused by the tips nanofocusing and gap plasmon coupling between the tips. A simple way to verify this electric field enhancement is to test SERS spectra when some analytes are chemisorbed onto the crescent-shaped nanostructures. Raman spectra of the crescent-shaped nanostructures with different morphologies, presented in **Figure 5**, were obtained by Raman spectrometer (LabRAM HR Evolution) with a non-polarized 633 nm excitation source. Figure S3, Supporting Information shows the calculated transmission spectra with different crescent nanostructures, the spectra demonstrate the resonant wavelength are near 633 nm, so the experimental source was selected with 633 nm to obtain the extremely strong SERS enhancement. Non-resonant paminothiophenol (PATP) molecules were used as probe molecules because they can form self-assembled monolayer (SAM) on the exposed gold surfaces.[1] Figure 5a shows Raman spectrum of PATP molecules, which were chemisorbed onto the crescent-shaped nanostructures with different morphologies. The Raman spectrum recorded from the CNGs was plotted by the blue curve in Figure 5a, the intensity is 1.7 times than that of CNWs (the black curve). It demonstrates the nanogap is important for the optical performance. Also, the Raman spectrum recorded on the OCNWs is represented by purple curve, whose Raman signal is 2.5 times compared to the CNWs. This observation suggests that OCNWs not only enlarge the tip density by introducing another crescent nanowire on the opposite side, but also improve the electric field intensity, which may be derived from tip nanofocusing at the crescent tips and
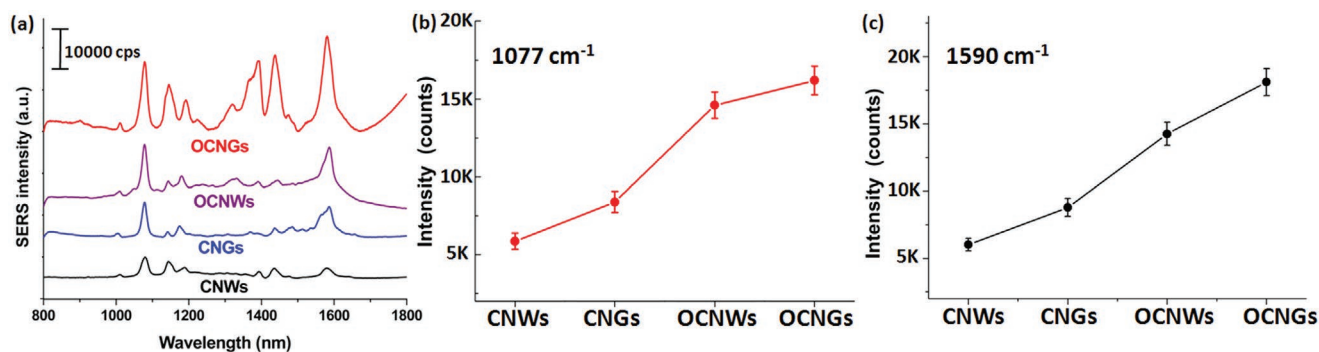

Figure 5. a) Experimentally recorded the Raman spectra of CNWs (black), CNGs (blue), OCNWs (purple) and OCNGs (red). b) Average SERS intensity at 1077 cm^{-1} of crescent nanostructures with different morphologies in (a) based on error bars. c) Average SERS intensity at 1590 cm^{-1} of crescent nanostructures with different morphologies in (a) based on error bars.

ADVANCED
SCIENCE NEWS
www.advancedsciencenews.com

ADVANCED
OPTICAL
MATERIALS
www.advopticalmat.de

the gap plasmon coupling between OCTs. Without consideration the interaction between the two OCTs, the total Raman intensity in the OCNWs (I_{OCNWs}) is the sum of the intensities of the two crescent nanowire (I_{CNWs}), that is, $I_{OCNWs} = 2 I_{CNWs}$. However, according to the above SERS experiments, the opposing crescent nanowires generated a more enhanced signal, $I_{OCNWs} = 2.5 I_{CNWs}$. The additional signal enhancement is attributed to the gap coupling between the two OCTs.

Moreover, the Raman signal intensity of OCNGs is 1.6 times compared with the OCNWs, which is indicated by the red curve. Ultimately, the nanogaps and opposing tips are the two key factors for optical performance enhancement. Figure 5b,c show the SERS intensities tendency at characteristic peaks with different crescent nanostructures, denotes as 1077 cm^{-1} and 1590 cm^{-1}. All Raman intensities were based on average with error bars. They both demonstrate that the SERS intensities with different morphologies show increasing trend, which is consistent with the calculated electric field enhancement. Further the results prove that the nanotips and nanogaps have a positive influence in electric field enhancement and Raman signal. Noted that the relative intensities of the Raman spectrum on the OCNGs substrate differ from the other, some of the characteristic peaks of PATP occur at around 1141, 1390, and 1435 cm^{-1}. These bands are enhanced by the charge transfer (CT) contributions.[53] We also calculated the enhancement factors (EF) for the four crescent nanostructures, the Raman spectrum of PATP molecule with 1 M chemisorbed on the flat Au substrate as a reference (Figure S4a, Supporting Information). Moreover, the Raman spectrum of PATP molecule with 1 M absorbed on the Si substrate is also given (Figure S4b, Supporting Information). The calculated EF is about 3.96×10^8 with CNWs, 5.64×10^8 with CNGs, 8.22×10^8 with OCNWs, 1.28×10^9 with OCNGs, respectively. This result proves that the OCNGs have great potential applications in SERS. In addition to the SERS Intensity, the uniformity is also important for reproducible SERS analysis. Figure S5, Supporting Information shows the Raman spectra measured from ten different locations of these crescent nanostructures. These SERS intensity is similar, indicating the repeatability for the as-prepared crescent nanostructures.
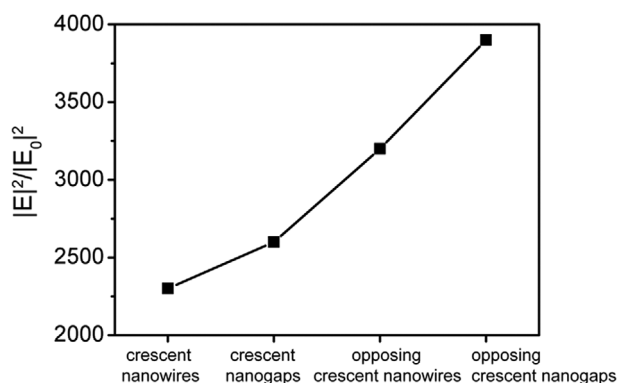
2.4. Electric Field Distributions of Crescent-shaped Nanostructures

In order to theoretically analyze the optical response of the fabricated structures, the gold crescent-shaped nanostructures on the gold film were modeled, and their near-field intensities were calculated using a 3D finite difference time-domain (FDTD) simulation. In the preparation of the model, the parameters of the nanostructures match those in the experiments. **Figure 6** shows electric field distributions illuminated by nonpolarized light for the crescent-shaped nanostructures in the x–y plane with different morphologies. The selected wavelength is 633 nm, which is consistent with experimental source. The monitors placed at air/Au nanostructures interface. Considering the geometric asymmetry of the crescent-shaped nanostructures, we investigated the influence of polarization light. Figures S6 and S7, Supporting Information demonstrate
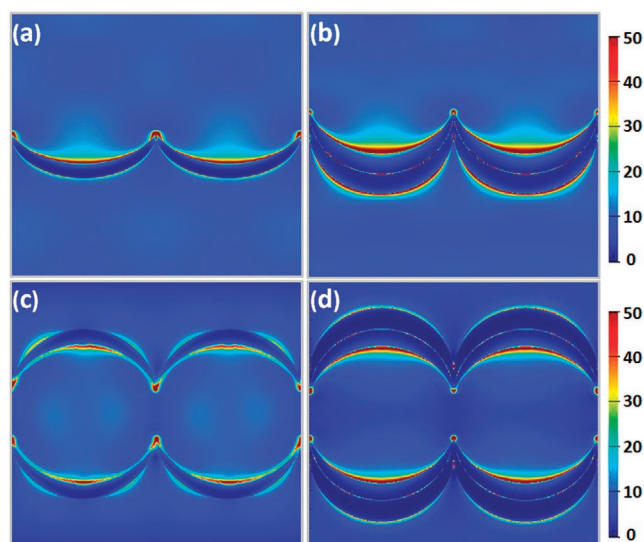
Figure 6. FDTD simulations of the electric field distributions $|E|^2/|E_0|^2$ of the crescents-shaped nanostructures with different morphologies excited by nonpolarized light.

the electric field polarized along the long axis and short axis, respectively. The electric field enhancements and distributions of the crescent-shaped nanostructures obtained by the orthogonal light polarization are significantly different. When the light is polarized along the long axis (Figure S6, Supporting Information), the electric field is primarily localized at the inner side of the crescent-shaped nanostructures. This observation is attributed to the higher-order quadrupole resonance modes (Left column of Figure S8, Supporting Information). Higher-order resonance modes can be clearly seen based on the charge distribution. In contrast, when light is polarized along the short axis (Figure S7, Supporting Information), the electric fields are localized at the sharp tips and along the backbone, which is attributed to the low-order resonance mode. As shown in right column of Figure S8, Supporting Information, dipole resonance modes occurred in the crescent-shaped nanostructures. FDTD simulations of the electric field distributions of the crescent-shaped nanostructures confirm the polarization-dependent optical behavior, which is consistent with previous report.[23] Compared with the electric field intensity when illuminated by long axis polarized light, the electric field intensity is higher than that when the light is polarized along the short axis. Because the electrons are equally distributed at both ends of the nanocrescents when the light is polarized along the long axis, where, as they move entirely to the sharp tips of the nanocrescents the light was polarized along the short axis, resulting in higher electric field enhancement. Noted that, the electric-field is largest in air/Au nanostructures interface (the electric-field intensity and distributions in the Au nanostructures/Au substrates interface of the CNWs is shown in Figure S9, Supporting Information). For more clearly, we simulated the electric field intensity and distribution of the crescent-shaped nanostructures on the y–z plane, the monitor is placed in the middle of the crescents (Figure S10, Supporting Information).

ADVANCED
SCIENCE NEWS
www.advancedsciencenews.com

ADVANCED
OPTICAL
MATERIALS
www.advopticalmat.de

Figure 7. Maximum of the calculated electric-field $|E|^2/|E_0|^2$ intensity as a function of different morphologies crescent-shaped nanostructures illuminated by unpolarized light.

In order to clearly demonstrate the maximum electric field enhancement, **Figure 7** shows the maximum $|E|^2/|E_0|^2$ intensity as a function of the different crescent-shaped nanostructures illuminated by unpolarized light. When illuminated by unpolarized light, the local maximum electric field intensity is approximately 3200 for OCNWs; the local maximum electric field intensity for CNGs can reach 2600, compared to the local maximum electric field intensity for CNWs of nearly 2300. The simulations are consistent with the experimental data. Moreover, for the OCNGs, the local maximum electric field intensity is about 3900, which indicates that the nanogaps and opposing tips will greatly enhance the electric field of the nanostructures. The large field enhancement is due to the tip-nanofocusing caused by the crescent tips and the gap plasmon coupling between the two gold crescent nanowires, in addition to, the extra gap plasmon coupling between the OCTs.

In conclusion, the nanogaps and the opposing sharp tips are two important components to the electric field enhancement. We should also mention that the tendency of the change to EM field is smaller than that of the SERS (Figure 5b), as the SERS intensity depends on $|E|^4$.[54] However, the SERS enhancement factor is less than the max enhancement ($|E|^4_{max}$), because the Raman probe molecules can attach anywhere along the y-axis of the crescent nanostructures and also the Raman signal is a weighted average.[43]

3. Conclusion

The combination of colloidal lithography and nanoskiving has been demonstrated as a simple, inexpensive, massively parallel, and materials/substrate-agnostic tool to fabricate high quality rows of crescent-shaped nanostructures with nanogaps and opposing sharp tips. Our method provides excellent control over the crescent-shape, tip spacing, nanogap size, and out-of-plane crescent height. One of the most intriguing results of this work is that rows of crescent nanogaps, opposing crescent nanowires, and opposing crescent nanogaps can be processed by colloidal lithography and nanoskiving. As far as we know, this is the first fabrication of opposing crescent nanostructures with nanogaps and opposing sharp tips. The rows of opposing

crescent nanogaps can be envisioned for various applications, such as fundamental studies of surface-enhanced Raman scattering, fluorescence enhancement, and cell imaging. Moreover, a variety of further implementations of opposing crescent structures in materials science can be expected. Any material with strong optical properties is a potential candidate.[55] The large electric field enhancement can further improve the sensing applications and nonlinear response of plasmonic materials.

4. Experimental Section

Materials: In the experiment, deionized water was ultrapure (18.2 MΩ·cm) from the Millipore water purification system. Ethanol was bought from Beijing Chemical Works and used without any treatment. The silicon wafers used as substrates were washed in piranha solution (7: 3 concentrated H_2SO_4/30% H_2O_2) at 120 °C for 1.5 h, to make the surface of silicon hydrophilic, and then repeatedly washed with deionized water and absolute ethanol. Noted that, the experiment must be carried out in a fume hood and the experimenter must wear rubber gloves, goggles, and gas masks. The silicon wafers were dried in a stream of nitrogen before use. Polystyrene (PS) spheres with diameter of 700 nm were bought from Wuhan Technology Co., Ltd. China. PDMS was bought from Dow Corning. Epoxy resin and hardener, polyethylene microtome mold were all bought from Electron Microscopy Sciences. The gold (99.999%) and aluminum for thermal vapor deposition were bought from Sinopharm Chemical Reagent Co., Ltd. The scotch tape was bought from 3M Co., Ltd. China.

Preparation of Monolayer Colloidal Crystals Film Templates: First, a chromium (Cr) adhesive layer of 3 nm was vertically deposited on the silicon wafer by a commercial thermal evaporation system (KYKY Technology Development Co., Ltd. China), the base pressure is 5×10^{-4} Pa and the deposition rate is 0.3–0.5 Å s^{-1}. Then, a single layer of hexagonal close packed (hcp) PS colloidal crystals with a diameter of 700 nm was self-assembled on the as-prepared substrate by the interface method. After that, an Au film of 110 nm was deposited vertically on the colloidal crystal samples with the base pressure of 5×10^{-4} Pa, and the deposition rate of 1.0–1.5 Å s^{-1}. After these procedures, the monolayer colloidal crystal film templates were fabricated.

Fabrication of CNWs: The epoxy pre-polymer (the volume ratio of epoxy resin and hardener is 15: 2) was dropped on the colloidal crystals film templates with a thickness of about 2 mm, and then cured in a drying oven at 60 °C for 6 h. After curing and peeling, the colloidal crystals film embedded in epoxy was obtained. The colloidal crystals film embedded in epoxy was cut out along the lattice direction using jeweler saws (cut into ≈2 × 10 mm^2 square millimeter block) and placed into separate holes of the polyethylene microtome mold, then filled with epoxy pre-polymer and cured. The epoxy blocks were fixed in the sample chuck of the ultra-microtome (Leica EM UC 7) and trimmed by a razor blade to define the embedded colloidal crystals film within an area of ≈2 × 2 mm^2. The blocks were sliced vertically at a speed of 0.6 mm s^{-1} with 100 nm thickness. After slicing, the slabs were transferred onto a gold film (0.5 × 0.5 mm^2). The slabs were then dried in an oven at 60 °C for 30 s to increase the adhesion between the slabs and the substrate. The thin epoxy slabs were etched by slight oxygen RIE. The inductively coupled plasma with 200 W power of Plasmalab Oxford 80 plus system (Oxford Instrument Co.) was used to etch for 15 min. After these steps, the CNWs were fabricated.

Fabrication of CNGs: The gold film of 110 nm was deposited on the colloidal crystals template. Then a aluminum film of 4 nm was deposited on the substrate, the base pressure of 5×10^{-4} Pa and the deposition rate of 0.3–0.5 Å s^{-1}. At the beginning of the deposition, bulk aluminum is melted with low current, and then the current increases gradually increased to obtain a relatively flat aluminum film. After that, another gold (110 nm) film was deposited on the substrate again. The epoxy

pre-polymer was dropped onto the colloidal crystals sandwich film templates with ≈2 mm thickness and then cured in an oven at 60 °C for 6 h. After curing and peeling, the colloidal crystals sandwich film embedded in epoxy was obtained. The colloidal crystals sandwich film embedded in epoxy was sectioned along the lattice direction using jeweler saws (cut into ≈2 × 10 mm² square millimeter bock) and placed into separate holes of the polyethylene microtome mold, then filled with epoxy pre-polymer, and cured. Then the epoxy blocks were fixed in the sample chuck of the ultra-microtome and trimmed by a razor blade to define the embedded colloidal crystals sandwich film structure within an area of ≈2 × 2 mm². The blocks were sliced vertically at a speed of 0.6 mm s⁻¹ with 100 nm thickness. After slicing, the slabs were transferred onto a gold film (0.5 × 0.5 mm²). The slabs were then dried at 60 °C to increase the adhesion between the slabs and the substrate. The sacrificial layer aluminum was removed by immersion in 2 mol L⁻¹ hydrochloric acid for 2 h. The thin epoxy slabs were etched by RIE. After these steps, the CNGs were fabricated.

Fabrication of OCNWs: First, the gold film of 110 nm was deposited on the colloidal crystals template. Then colloidal crystals film was peeled off by scotch tape. Another gold film of 110 nm was deposited on the opposite side of the colloidal crystals film template. The epoxy pre-polymer was dropped onto the colloidal crystals opposite film templates with ≈2 mm thickness and then cured in a drying oven at 60 °C for 6 h. After curing and peeling, a colloidal crystal opposite film embedded in epoxy was obtained. The colloidal crystals opposite film embedded in epoxy was cut out along the lattice direction using jeweler saws and placed into separate holes of the polyethylene microtome mold, then filled with epoxy pre-polymer, and cured. Then the epoxy blocks were fixed in the sample chuck of the ultra-microtome and trimmed by a razor blade to define the embedded colloidal crystals opposite film structure within an area of ≈2 × 2 mm². The blocks were vertically sectioned at a speed of 0.6 mm s⁻¹ with 100 nm thickness. After slicing, the slabs were transferred onto a gold film. The slabs were then dried at 60 °C to increase the adhesion between the slabs and the substrate. The thin epoxy film was etched by RIE. After these steps, the OCNWs were fabricated.

FDTD Simulations: The electric field distributions and transmission spectra were calculated using a 3D finite difference time-domain (FDTD) solutions (Lumerical Solutions Inc. Canada). In the model preparation, the parameters of the nanostructures match those in the experiments. The selected excitation source was 633 nm. Monitors of frequency-domain field profile were located in x–y plane and y–z plane. In order to obtain accurate results, the auto nonuniform mesh with mesh accuracy 4 was applied in simulation. The range of simulated transmission spectra was 300–800 nm. The optical parameters of Au and Si were selected from Palik's handbook.

Characterization: The concentrations of the probe molecule (PATP) was 1×10^{-3} M, however the diluted PATP solution for flat Au film was 1 M. All measuring samples were soaked in analyte solution with 12 h, and then samples were rinsed with ethanol to remove extra analyte. The model of Raman is LabRAM HR Evolution. The selected excitation source is 633 nm to consistent with the simulation. The transmittance is 1%. The range of beam spot is 1000 nm. The exposure time was selected as 10 s.

Supporting Information

Supporting Information is available from the Wiley Online Library or from the author.

Acknowledgements

Conflict of Interest

The authors declare no conflict of interest.

[1] M. Chirumamilla, A. Toma, A. Gopalakrishnan, G. Das, R. P. Zaccaria, R. Krahne, E. Rondanina, M. Leoncini, C. Liberale, F. De Angelis, E. Di Fabrizio, *Adv. Mater.* **2014**, *26*, 2353.

[2] S. Si, W. Liang, Y. Sun, J. Huang, W. Ma, Z. Liang, Q. Bao, L. Jiang, *Adv. Funct. Mater.* **2016**, *26*, 8137.

[3] H.-J. Jang, I. Jung, L. Zhang, S. Yoo, S. Lee, S. Cho, K. L. Shuford, S. Park, *Chem. Mater.* **2017**, *29*, 5364.

[4] H. Zhang, M. Liu, F. Zhou, D. Liu, G. Liu, G. Duan, W. Cai, Y. Li, *Small* **2015**, *11*, 844.

[5] H. Zhang, F. Zhou, M. Liu, D. Liu, D. Men, W. Cai, G. Duan, Y. Li, *Adv. Mater. Interfaces* **2015**, *2*, 1500031.

[6] D. Liu, C. Li, F. Zhou, T. Zhang, H. Zhang, X. Li, G. Duan, W. Cai, Y. Li, *Sci. Rep.* **2015**, *5*, 7686.

[7] K. M. Mayer, J. H. Hafner, *Chem. Rev.* **2011**, *111*, 3828.

[8] C. Gao, Z. Lu, Y. Liu, Q. Zhang, M. Chi, Q. Chen, Y. Yin, *Angew. Chem., Int. Ed.* **2012**, *51*, 5629.

[9] S. Klinghammer, T. Uhlig, F. Patrovsky, M. Böhm, J. Schütt, N. Pütz, L. Baraban, L. M. Eng, G. Cuniberti, *ACS Sens.* **2018**, *3*, 1392.

[10] H. Aouani, M. Rahmani, M. Navarro-Cia, S. A. Maier, *Nat. Nanotechnol.* **2014**, *9*, 290.

[11] M. Celebrano, X. Wu, M. Baselli, S. Grossmann, P. Biagioni, A. Locatelli, C. De Angelis, G. Cerullo, R. Osellame, B. Hecht, L. Duo, F. Ciccacci, M. Finazzi, *Nat. Nanotechnol.* **2015**, *10*, 412.

[12] R. B. DavidsonII, A. Yanchenko, J. I. Ziegler, S. M. Avanesyan, B. J. Lawrie, R. F. Haglund Jr., *ACS Photonics* **2016**, *3*, 1477.

[13] Z. Zhang, B. Zhou, Y. Huang, Z. Liao, Z. Li, S. Li, S. Wang, W. Wen, *Appl. Opt.* **2014**, *53*, 7236.

[14] T. K. Sau, A. L. Rogach, F. Jackel, T. A. Klar, J. Feldmann, *Adv. Mater.* **2010**, *22*, 1805.

[15] C. Clavero, *Nat. Photonics* **2014**, *8*, 95.

[16] C. Wang, D. Astruc, *Chem. Soc. Rev.* **2014**, *43*, 7188.

[17] K. Li, N. J. Hogan, M. J. Kale, N. J. Halas, *Nano Lett.* **2017**, *17*, 3710.

[18] X. Yang, M. Yang, B. Pang, M. Vara, Y. Xia, *Chem. Rev.* **2015**, *115*, 10410.

[19] Y. Hu, X. Liu, Z. Cai, H. Zhang, H. Gao, W. He, P. Wu, C. Cai, J. -J. Zhu, Z. Yan, *Chem. Mater.* **2019**, *31*, 471.

[20] B. Luk'yanchuk, N. I. Zheludev, S. A. Maier, N. J. Halas, P. Nordlander, H. Giessen, C. T. Chong, *Nat. Mater.* **2010**, *9*, 707.

[21] B. Zhou, X. Xiao, T. Liu, Y. Gao, Y. Huang, W. Wen, *Biosens. Bioelectron.* **2016**, *77*, 385.

[22] Q. Wang, L. L. Yu, C. J. Liu, X. L. Xu, *EPL Europhys. Lett.* **2017**, *118*, 64002.

[23] X. M. Zhang, J. J. Han, Q. Zhang, F. F. Qin, J. J. Xiao, *Opt. Commun.* **2014**, *325*, 9.

[24] R. Bukasov, J. S. Shumaker-Parry, *Anal. Chem.* **2009**, *81*, 4531.

[25] C. T. Cooper, M. Rodriguez, S. Blair, J. S. Shumaker-Parry, *J. Phys. Chem. C* **2015**, *119*, 11826.

[26] M. Swartz, M. Rodriguez, A. D. Quast, C. T. Cooper, S. Blair, J. S. Shumaker-Parry, *J. Phys. Chem. C* **2016**, *120*, 20597.

ADVANCED
SCIENCE NEWS

www.advancedsciencenews.com

ADVANCED
OPTICAL
MATERIALS

www.advopticalmat.de

[27] C. J. Zheng, T. Q. Jia, H. Zhao, Y. J. Xia, S. Zhang, D. H. Feng, Z. R. Sun, *Plasmonics* **2018**, *13*, 1121.

[28] A. I. Fernandez-Dominguez, Y. Luo, A. Wiener, J. B. Pendry, S. A. Maier, *Nano Lett.* **2012**, *12*, 5946.

[29] H. Yang, B. Q. Li, X. Jiang, W. Yu, H. Liu, *Nanotechnology* **2017**, *28*, 505301.

[30] J. S. Shumaker-Parry, H. Rochholz, M. Kreiter, *Adv. Mater.* **2005**, *17*, 2131.

[31] J. Fischer, N. Vogel, R. Mohammadi, H. J. Butt, K. Landfester, C. K. Weiss, M. Kreiter, *Nanoscale* **2011**, *3*, 4788.

[32] N. Vogel, J. Fischer, R. Mohammadi, M. Retsch, H. J. Butt, K. Landfester, C. K. Weiss, M. Kreiter, *Nano Lett.* **2011**, *11*, 446.

[33] R. Bukasov, T. A. Ali, P. Nordlander, J. S. Shumaker-Parry, *ACS Nano* **2010**, *4*, 6639.

[34] H. Jiang, J. Markowski, J. Sabarinathan, *Opt. Express* **2009**, *17*, 21802.

[35] Z. A. Lewicka, Y. Li, A. Bohloul, W. W. Yu, V. L. Colvin, *Nanotechnology* **2013**, *24*, 115303.

[36] L. Gao, L. Lin, J. Hao, W. Wang, R. Ma, H. Xu, J. Yu, N. Lu, W. Wang, L. Chi, *J. Colloid Interface Sci.* **2011**, *360*, 320.

[37] Z. Li, X. Zhang, S. Ye, J. Zhang, T. Wang, L. Fang, J. Zhang, B. Yang, *Nanotechnology* **2013**, *24*, 105307.

[38] T. Wang, J. Zhang, P. Xue, H. Chen, S. Ye, S. Wang, Y. Yu, B. Yang, *J. Mater. Chem. C* **2014**, *2*, 2333.

[39] Z. Wang, B. Ai, Z. Zhou, Y. Guan, H. Mohwald, G. Zhang, *ACS Nano* **2018**, *12*, 10914.

[40] Y. Cai, Z. Zhao, J. Chen, T. Yang, P. S. Cremer, *ACS Nano* **2012**, *6*, 1548.

[41] Q. Xu, R. M. Rioux, M. D. Dickey, G. M. Whitesides, *Acc. Chem. Res.* **2008**, *41*, 1566.

[42] P. Pourhossein, R. K. Vijayaraghavan, S. C. Meskers, R. C. Chiechi, *Nat. Commun.* **2016**, *7*, 11749.

[43] L. Jibril, J. Ramirez, A. V. Zaretski, D. J. Lipomi, *Sens. Actuators, A* **2017**, *263*, 702.

[44] W. Zhang, P. Gu, Z. Wang, B. Ai, Z. Zhou, Z. Zhao, C. Li, Z. Shi, G. Zhang, *Adv. Opt. Mater.* **2019**, *7*, 1901337.

[45] J. Rybczynski, U. Ebels, M. Giersig, *Colloids Surf. A* **2003**, *219*, 1.

[46] B. Ai, Y. Yu, H. Moehwald, L. Wang, G. Zhang, *ACS Nano* **2014**, *8*, 1566.

[47] D. Liu, F. Zhou, C. Li, T. Zhang, H. Zhang, W. Cai, Y. Li, *Angew. Chem., Int. Ed.* **2015**, *54*, 9596.

[48] P. Gu, Z. Zhou, Z. Zhao, H. Mohwald, C. Li, R. C. Chiechi, Z. Shi, G. Zhang, *Nanoscale* **2019**, *11*, 3583.

[49] Z. Zhou, Z. Zhao, Y. Yu, B. Ai, H. Mohwald, R. C. Chiechi, J. K. Yang, G. Zhang, *Adv. Mater.* **2016**, *28*, 2956.

[50] X. Chen, H. R. Park, M. Pelton, X. Piao, N. C. Lindquist, H. Im, Y. J. Kim, J. S. Ahn, K. J. Ahn, N. Park, D. S. Kim, S. H. Oh, *Nat. Commun.* **2013**, *4*, 2361.

[51] H. Cai, Q. Meng, H. Zhao, M. Li, Y. Dai, Y. Lin, H. Ding, N. Pan, Y. Tian, Y. Luo, X. Wang, *ACS Appl. Mater. Interfaces* **2018**, *10*, 20189.

[52] V. E. Bochenkov, D. S. Sutherland, *Nano Lett.* **2013**, *13*, 1216.

[53] Y. Wang, W. Ji, Z. Yu, R. Li, X. Wang, W. Song, W. Ruan, B. Zhao, Y. Ozaki, *Phys. Chem. Chem. Phys.* **2014**, *16*, 3153.

[54] P. Alonso-Gonzalez, P. Albella, M. Schnell, J. Chen, F. Huth, A. Garcia-Etxarri, F. Casanova, F. Golmar, L. Arzubiaga, L. E. Hueso, J. Aizpurua, R. Hillenbrand, *Nat. Commun.* **2012**, *3*, 684.

[55] D. J. Lipomi, R. V. Martinez, R. M. Rioux, L. Cademartiri, W. F. Reus, G. M. Whitesides, *ACS Appl. Mater. Interfaces* **2010**, *2*, 2503.

2000006 (8 of 8)